Space Sci Rev
DOI 10.1007/s11214-008-9440-2

The THEMIS ESA Plasma Instrument and In-flight Calibration

J.P. McFadden · C.W. Carlson · D. Larson · M. Ludlam · R. Abiad · B. Elliott · P. Turin · M. Marckwordt · V. Angelopoulos

Received: 28 February 2008 / Accepted: 16 September 2008
© Springer Science+Business Media B.V. 2008

Abstract The THEMIS plasma instrument is designed to measure the ion and electron distribution functions over the energy range from a few eV up to 30 keV for electrons and 25 keV for ions. The instrument consists of a pair of "top hat" electrostatic analyzers with common $180° \times 6°$ fields-of-view that sweep out 4π steradians each 3 s spin period. Particles are detected by microchannel plate detectors and binned into six distributions whose energy, angle, and time resolution depend upon instrument mode. On-board moments are calculated, and processing includes corrections for spacecraft potential. This paper focuses on the ground and in-flight calibrations of the 10 sensors on five spacecraft. Cross-calibrations were facilitated by having all the plasma measurements available with the same resolution and format, along with spacecraft potential and magnetic field measurements in the same data set. Lessons learned from this effort should be useful for future multi-satellite missions.

Keywords THEMIS · Space plasma instrument · Calibrations · Electrostatic analyzer · In-flight calibrations

PACS 94.80.+g · 06.20.fb · 94.30.C- · 94.05.-a · 07.87.+v

1 Introduction

The THEMIS mission was designed to study fundamental processes concerning the nature of magnetospheric substorms, the explosive release of solar wind energy stored in the Earth's magnetotail (Sibeck and Angelopoulos 2008). To address the substorm problem, the THEMIS team built five identical spacecraft which were placed in highly-elliptical near-equatorial orbits with apogees of $\sim$11.8 Re for the three inner probes, and apogees of $\sim$19.6

J.P. McFadden (✉) · C.W. Carlson · D. Larson · M. Ludlam · R. Abiad · B. Elliott · P. Turin · M. Marckwordt · V. Angelopoulos
University of California, Berkeley, USA
e-mail: mcfadden@ssl.berkeley.edu

V. Angelopoulos
University of California, Los Angeles, USA

and ∼31.6 Re for the outer probes (Angelopoulos 2008). Orbital periods for the probes are 1, 2 and 4 days allowing magnetotail alignment conjunctions once every 4 days as required for substorm timing analysis.

THEMIS was launched on February 17, 2007, into an initial insertion orbit with an apogee of 14.7 Re near ∼ 21 MLT and shifting to the dayside with the Earth's orbital motion. This orbit required a 7 month coast phase, where the spacecraft were kept in a close configuration to keep orbital parameters optimized for final orbit insertion in the fall of 2007. This close proximity allowed accurate cross-calibration of the plasma instruments as described in Sect. 2 in preparation for the substorm campaign in early 2008. In addition, "First results" papers in this issue are primarily concerned with dayside science investigations. First results from the plasma sensors, along with other performance issues, can be found in the companion paper, McFadden et al. (2008).

Each THEMIS spacecraft (Harvey et al. 2008) contains a fluxgate magnetometer (Auster et al. 2008), a search-coil magnetometer (Roux et al. 2008), electric field instrument (Bonnell et al. 2008), solid state telescopes (Larson et al. 2008) and the ESA (Electro-Static Analyzer) plasma instrument described below. These core instruments provide a set of measurements needed to resolve the in-situ dynamics of substorms. The plasma instrument provides detailed ion and electron particle distribution function measurements along with on-board moment calculations. The overall mechanical and electrical design of the THEMIS ESA plasma instrument was directly derived from the FAST Plasma Instrument (Carlson et al. 2001). Below we present a description of the instrument technical design and data products, followed by an in depth discussion of the calibrations. Lessons learned from this calibration effort should be useful for future multi-satellite missions.

1.1 Sensor Description

The THEMIS plasma instrument consists of a pair of top-hat electrostatic analyzers (ESAs) (Carlson et al. 1983) that measure ion and electron energy per charge (E/q). Figure 1 shows a picture and cross-section of the sensors which are packaged together to provide a common field-of-view (FOV). The electron and ion analyzers have $\Delta R/R$ of 0.060 and 0.075, respectively, with inherent energy resolutions of about 15% and 19%. The sensors have

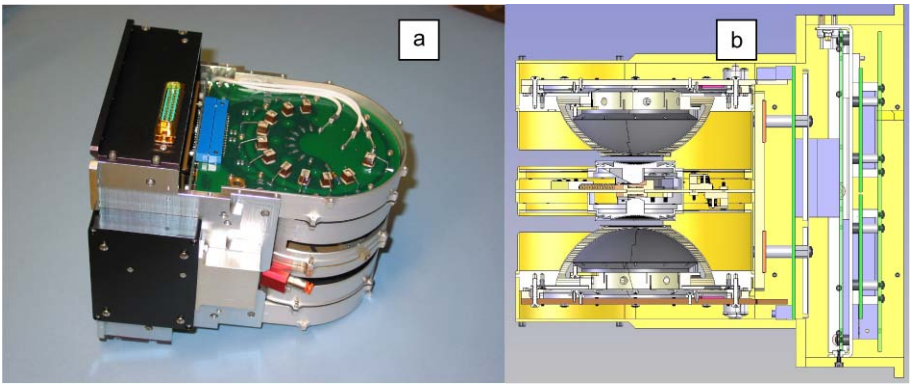

Fig. 1 The THEMIS ion and electron Electrostatic Analyzers (ESAs) are packaged together to provide a common field of view. (**a**) ESA with the anode cover removed reveals coupling capacitors. The LVPS (*black*) is mounted on the side and the nitrogen purge inlet (*red*) is exposed. (**b**) Analyzer cutaway shows the common aperture mechanism and electronics packaging

selectable energy sweeps (programmable starting energy with logarithmic or linear sweep steps) and are generally swept in energy (logarithmically) from ∼32 keV for electrons and ∼25 keV for ions, down to ∼6–7 eV. Nominal operations have 32 sweeps per spin, with 31 energy samples per sweep, plus one sample energy retrace, resulting in a typical measurement resolution with $\Delta E/E \sim 32\%$. Particle events are registered by microchannel plate (MCP) detectors.

Both sensors have a 180° × 6° FOV (FWHM), with the 6° rotating with the spacecraft to provide 4π steradian coverage each spin. 32 sweeps per spin provides 11.25° resolution in rotation phase (ϕ). The electron sensor has 8 anodes giving 22.5° resolution in the polar angle (θ), while the ion sensor has 16 anodes with up to 5.625° resolution. The high angular resolution anodes in the ion sensor are concentrated at the spin plane to resolve solar wind ions. The ion sensor can also be operated in a double-sweep mode (64 sweeps/spin, 16 energies) to provide a similar 5.625° angular resolution in rotation phase.

Table 1 summarizes the electron and ion instrument specifications. Geometric factors are for 180° FOV sensors and include energy acceptance such that differential flux, $(\mathrm{s\,cm^2\,sr\,eV})^{-1}$, is given by count rate divided by geometric factor at the given energy "E". A typical count binning pixel has 1/8 of this geometric factor (22.5°/180°), with two sweeps (1/16 spin) contributing to a pixel, or 6 ms accumulation time per energy sample. The in-flight calibrations indicate the measured geometric factors are roughly equal to the predicted geometric factors. Predicted geometric factors are from simulations, combined with grid losses and assumed MCP efficiency. The discrepancies are likely due to a combination of internal scattering and leakage fields near the analyzer exit. Leakage fields through an exit grid and into the analyzer, caused by a bias voltage applied to the front of the MCP detectors, can increase the sensor's response at low energies as discussed in Sect. 2.2.

Figure 2 illustrates the ESA plasma instrument's modular design which allows subassemblies to be constructed and tested separately. Figure 2a shows the MCP (red) detectors and mounting hardware that attach to the anode. Spring fingers on both the inner and outer edges of the MCP annulus distribute the force providing uniform clamping that can withstand ∼85 Gs of acceleration. This subassembly allows MCP testing and characterization prior to sensor assembly. The tab on the lower right corner of the anode is the interface to the purge tube that supplies filtered dry nitrogen during storage. Figure 2b reveals an analyzer design that maintains its concentricity to ∼15 μm under normal assembly. Although the hemisphere alignment is controlled by three interfaces, the flexible insulator that supports the inner hemisphere is self-centering producing an alignment equivalent to the tolerance at the outer mounting plate interface.

The outer hemisphere was serrated and all internal surfaces were blackened with ebanol-C to reduce scattered sunlight from reaching the detectors. (Ebanol-C is found to reduce scattered sunlight by at least a factor of 10 over gold-black, which was used on the FAST satellite.) Figure 2c shows the combined anode, analyzer, outer aperture, and the top-hat. The top-hat is supported by a torsion spring and contains a conductive gasket that seals against the outer hemisphere during launch to prevent contamination. Figure 2d shows the release plate mechanism that pushes both ion and electron sensor top-hats into closed positions against their outer hemispheres. The reset-able, SMA-actuator release mechanism was developed for the THEMIS program to simplify sensor refurbishment during ground testing, replacing a melt-wire design used for the FAST mission. The release mechanism also acts as a poppet valve during nitrogen purge and rocket ascent, preventing over-pressure by venting gas at the top-hat.

The modular design also extends to the ESA electronics as illustrated in Fig. 3. The instrument simplifies assembly by eliminating most of the harnessing by coordinating the

Table 1 ESA instrument specifications

Parameter	Value	Comments
Electron electrostatic analyzer		Spherical top-hat
$\Delta R/R$	0.06	37.5 mm inner hemisphere radius
Analyzer constant	7.9	0 to 4 kV sweep supply
Energy range	2 eV to 32 keV	
Analyzer energy resolution	17% (15%)	$\Delta E/E$ measured (predicted)
Measurement energy resolution	32%	Typical 31 step log energy sweep
Energy sweep rate	32 per spin	~94 ms for nominal 3 s spin
Instantaneous field of view	180° × 6° FWHM	180° centered on spin plane
Anode angle resolution	22.5°	8 anodes
Field of view each spin	4π	steradians
Analyzer geometric factor	0.0075 cm^2 sr E	Predicted from simulations, analyzer only
	0.0047 cm^2 sr E	One 90% exit grid and 70% MCP efficiency
Sensor geometric factor	0.0066 cm^2 sr E	From in-flight calibration, includes grid losses, MCP efficiency @10 eV
Counter readout	1024 per spin	~3 ms
Full distribution array	32E×88Ω	32 or 128 spin cadence, continuous
Burst distribution array	32E×88Ω	1 spin cadence, 30–60 min/orbit
Reduced distribution array	32E×6Ω or	1 spin cadence, continuous, 6Ω in FS mode
	32E×1Ω	1Ω in SS mode
Ion electrostatic analyzer		Spherical top-hat
$\Delta R/R$	0.075	37.5 mm inner hemisphere radius
Analyzer constant	6.2	0 to 4 kV sweep supply
Energy range	1.6 eV to 25 keV	
Analyzer energy resolution	18% (19%)	$\Delta E/E$ measured (predicted)
Measurement energy resolution	32%	Typical 31 step log energy sweep
Energy sweep rate	32 or 64 per spin	64/spin in solar wind mode with 16 energies
Instantaneous field of view	180° × 6° FWHM	180° centered on spin plane
Anode angle resolution	5.6 ° to 22.5°	16 anodes
Field of view each spin	4π	steradians
Analyzer geometric factor	0.0181 cm^2 sr E	Predicted from simulations, analyzer only
	0.0073 cm^2 sr E	Two 90% grids and 50% MCP efficiency
Sensor geometric factor	0.0061 cm^2 sr E	From in-flight calibration, includes grid losses and MCP efficiency @500 eV
Counter readout	1024 per spin	~3 ms
Full distribution array	32E ×88Ω	32 or 128 spin cadence, continuous
Burst distribution array	32E ×88Ω	1 spin cadence, 30–60 min/orbit
Reduced distribution array	24E×50Ω or	1 spin cadence, continuous, 50Ω in FS mode
	32E×1Ω	1Ω in SS mode

mechanical and electrical designs. Figures 3a and 3b show the preamplifier board which contains 24 Amptek A121 preamplifiers for both sensors. This board uses a single FPGA to implement counters and a command decoder that controls its test pulser and the preamplifier

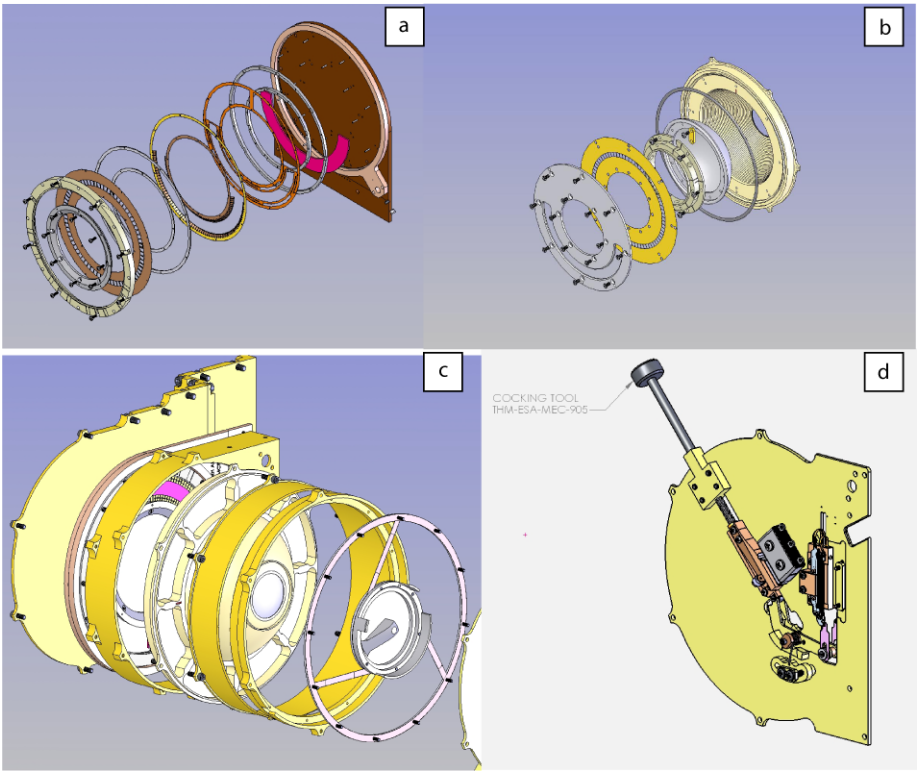

Fig. 2 (**a**) THEMIS detector-anode module, (**b**) analyzer module, (**c**) sensor subassembly, and (**d**) the aperture release plate mechanism with SMA actuator. The modular mechanical design allowed subsystem assembly and testing to proceed in parallel for the 10 ESA sensors

gains. Separate high voltage (HV) boards are used for electron and ion sensors, each board (Fig. 3c) containing a raw sweep supply and MCP supply for a single sensor. The HV boards mount to a common mechanical frame (Fig. 3d) that also supports the Interface-Sweep (IS) board (Fig. 3e) and a small mother board (Fig. 3d) that provides an electrical interface between the IS and HV boards. The IS board contains opto-coupler (Amptek HV601) circuits for analyzer HV sweeps, in addition to providing FPGA control voltages for the sweeps and the HV boards. The combined electron–ion instrument requires two +28 V power lines, one for low voltage (LV) and one for HV. Figure 3f shows the LV power supply which mounts to the side of the ESA instrument.

The ESA interfaces to the Instrument Data Processing Unit or IDPU (Taylor et al. 2008) which provides power, control, and data interfaces. Figure 4 shows a block diagram of the ESA. MCP detectors in chevron configuration are voltage biased at $\sim$2 kV to amplify input events to $\sim 2 \times 10^6$ e^-, approximately -320 fC. Amptek A121 preamplifiers are used to detect output charge pulses and have programmable gain to facilitate testing. Events are recorded by counters which are read out 1024 times per spin. The ESA electronics include a programmable test pulse generator to provide electronic stimulation when high voltage is off. The rate of this stimulation can be slaved to the analyzer sweep control to confirm internal timing. For nominal operation the preamplifier thresholds are set at -40 fC ($\sim$250,000 electrons), well above electronic noise in the system. For MCP gain testing, the

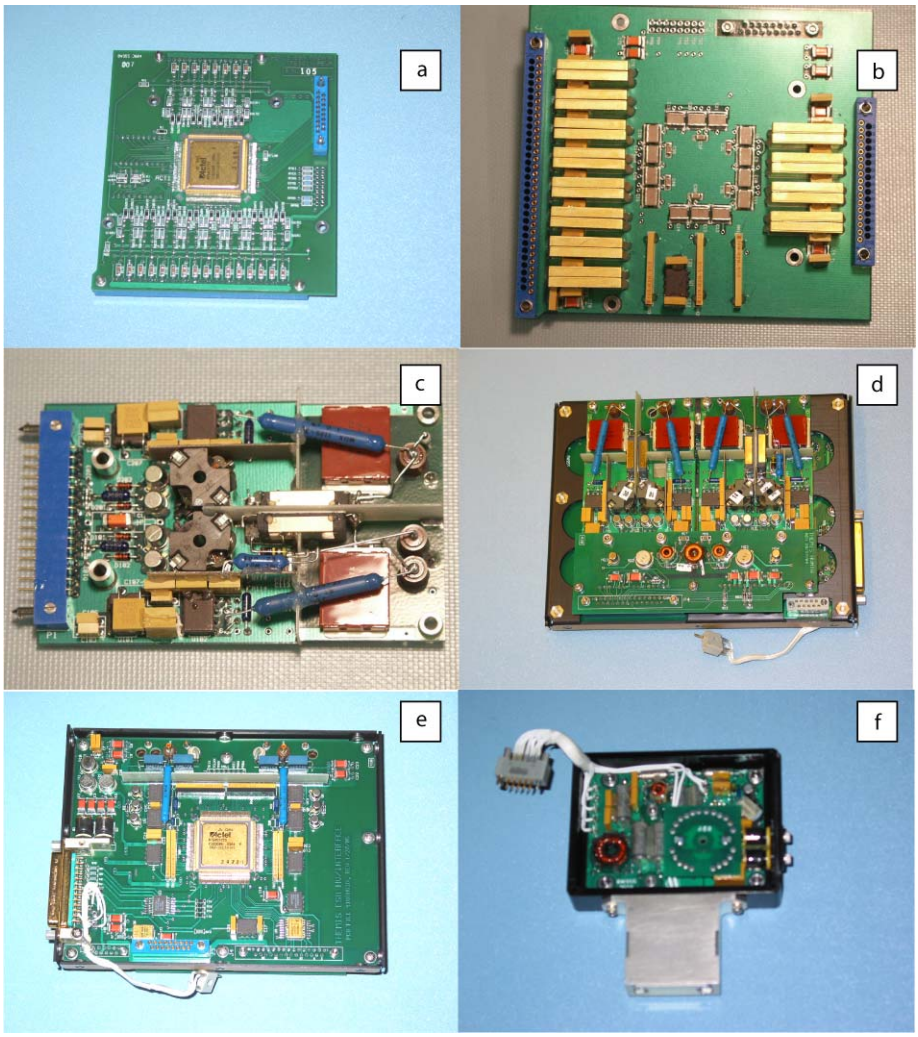

Fig. 3 The THEMIS ESA electronics shown here includes the preamplifier board, with front (**a**) and back (**b**) views, the paired sweep and MCP high voltage power supplies shown individually (**c**) or mounted to the back of the interface and sweep control board (**d**) along with the ESA mother board, the front of the interface and sweep control board (**e**), and the low voltage power supply (**f**). The modular mechanical-electrical design minimized harnessing, allowing quick assembly and disassembly of the instruments

preamplifier gain is toggled, switching the threshold from −40 fC to −330 fC several times. A factor of two change in count rate indicates the peak in the MCP's pulse height distribution is about −330 fC, the desired 2×10^6 gain.

As mentioned above, the ESA contains four separate high voltage power supplies (HVPS), two for MCPs and two for the ion and electron energy sweeps. All HVPS are separately controlled by the IDPU to allow independent operation of both sensors. The sweep supplies produce a 5 kV maximum output (−5 kV for ions), that is used as a raw input to an opto-coupler circuit that provides voltage to the inner hemispheres. The hemispheres are swept from high voltage to low voltage in ∼100 ms, with ∼1 ms required for the high volt-

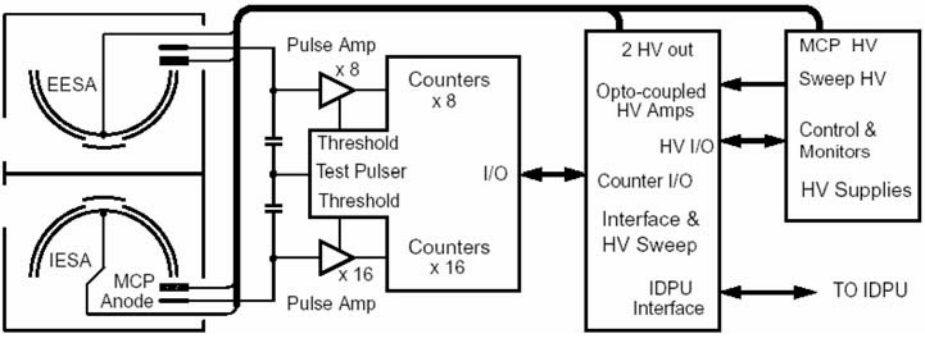

Fig. 4 THEMIS ESA block diagram

age to retrace to its starting value. The energy sweep is synchronized to the 1024 pulse/spin input clock that also controls counter readout.

1.2 ESA Modes and Data Products

ESA data are collected and formatted by the ETC board in the IDPU into seven data products: two full packets, two burst packets, two reduced packets, and moment packets. Each sensor has separate packets, except for moment packets which are made by combining data from both ESAs and the Solid State Telescopes (SSTs) (Larson et al. 2008). The format of each data product is programmable and may change with time depending on the "Spacecraft-Mode", the location within the magnetosphere, or with the development of new "instrument-modes" that can be uploaded to the satellites. Below we describe data products generated by the nominal "magnetospheric mode" used for the majority of the first nine months of the mission, and the "solar wind" mode which can be used to resolve the cold solar wind ions.

"Full packets" are a low-time-resolution data product useful for large scale surveys of THEMIS data. They generally maintain the "full" 32 energies sampled, and have an 88 solid-angle map as illustrated in Fig. 5a. Full distribution data are 1-spin snapshots of the plasma with a measurement cadence of either 32 spins (in "Fast-Survey Spacecraft-Mode") or 128 spins ("Slow-Survey Spacecraft-Mode"). These high energy-angle resolution measurements are the primary data product used for the in-flight calibration effort described below. Full packets are used to generate summary plots, to validate the on-board plasma moment computations, and to provide detailed distribution functions in all regions of the magnetosphere. Full distribution data are particularly helpful for the identification of unique features, such as counter-streaming field-aligned beams, that may not be easily identified from other data products such as moments. Different angle maps can be selected for full packets in different region of space. Figure 5b illustrates the angle map for a "solar wind" spacecraft mode which provides $\sim 5.6^\circ$ resolution for solar wind beams.

"Burst packets" contain high-resolution 3-D plasma distribution functions with spin-period time resolution. Due to telemetry limitations, burst packets are generally limited to several five-minute-intervals each orbit. Burst packet format is usually the same as full packet format, with 32 energies and 88 solid angles. The selected time intervals are chosen by ground command or by on-board triggers as discussed in Angelopoulos (2008). Burst data provide the high resolution measurements needed to resolve boundary crossings such as the magnetotail neutral sheet, plasma sheet boundary layer, magnetopause, and bow shock.

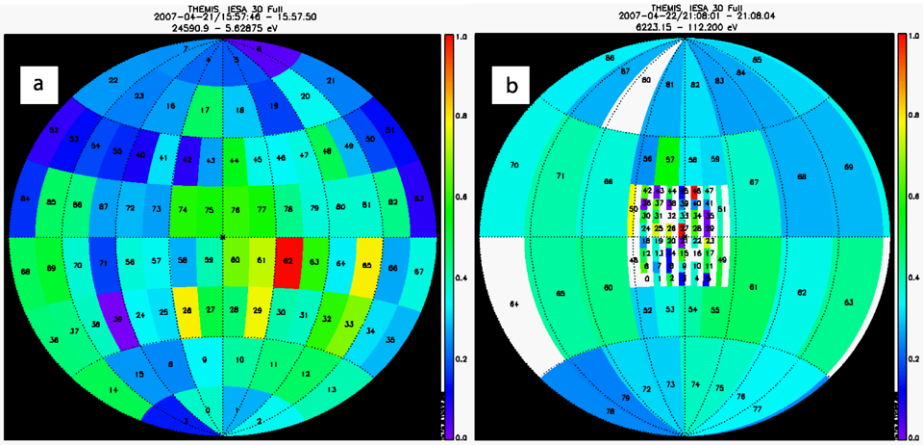

Fig. 5 (**a**) Typical 88 solid-angle map used for collecting both ion and electron ESA data into full and burst data packets in the magnetosphere. (**b**) Ion angle map used for ion solar wind mode packets, where only bins 0–87 are labeled. Bins 88–175 are shifted 5.6 degrees to the right of bins 0–87 and have bin numbers given by the adjacent bin plus 88. Angle maps are programmable allowing different anodes and sweeps to be combined to produce solid angle resolution that support a particular science goal

"Reduced packets" are 1-spin-resolution plasma distributions sampled continuously, but with limited solid-angle and/or energy coverage. When in Slow-Survey mode, reduced packets are generally composed of 32-energy, omni-directional spectra which allow energy-time spectrograms with the same cadence as on-board moment data. In Fast-Survey mode, the nominal ion reduced packet consists of a 24-energy, 50-solid-angle distribution, while the electron reduced packet is a 32-energy, 6-solid-angle distribution (see Fig. 6). These Fast-Survey mode formats were chosen to maintain enough angular information so that plasma moments could be computed and so features of the distribution, such as field-aligned beams, could be deduced. When combined with on-board spin-resolution moment data, reduced data allows high-time resolution science investigations to be conducted on data gathered throughout the orbit.

"Moment packets" contain spin-resolution on-board computations of the ion and electron ESA and SST (> 30 keV) moments. These moments include the plasma density, three components of flux, six components of the momentum tensor, and 3 components of energy flux, computed separately for the four instruments (iESA, eESA, iSST, eSST). These partial moments can be combined on the ground to get the total moments, or combined to calculate related quantities such as velocity and pressure. Combining ESA and SST data can be especially important for determining the total pressure in the plasma sheet. THEMIS on-board moment calculations are unique in that THEMIS is the first mission to include corrections for spacecraft charging. Spacecraft potential, as measured by the EFI instrument (Bonnell et al. 2008), is used to correctly shift the energies of particles in the moment computations. In particular this correction eliminates photo-electrons which often contaminate electron plasma measurements. Moment computations also include weighting factors to correct for energy and angle efficiency variations in the sensors.

1.3 Ground Testing and Calibrations

In addition to standard functional tests, ground testing of the ESA sensors included several subsystem optimizations prior to assembly and calibration. Before loading into flight

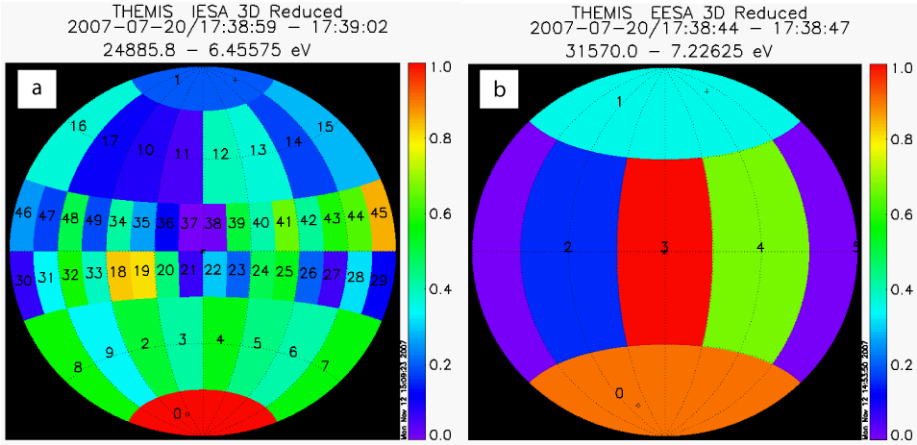

Fig. 6 Typical ion (*left*) and electron (*right*) solid angle maps showing angle bin number for reduced data packets during fast survey magnetospheric mode. Color coding is in normalized counts. Reduced data are produced at spin resolution and maintain 32 energies for electrons and 24 energies for ions. The 50 solid angles for the ions are adequate for accurate velocity moments except during narrow beams along the spin axis. The 6 solid angles for electrons are adequate to identify anisotropies such as counter-streaming electrons

boards, A121 preamplifiers were individually tested for response including threshold, output pulse length and dead time to assure nearly identical characteristics for all amplifiers. Optocoupler high voltage sweep electronics were tuned to provide near zero offset at the lowest DAC control setting (actual voltage offsets were < 10 mV on a 4 kV output), to provide nearly identical ($\sim 1\%$) high voltage control gain, and to have rapid settling ($\sim$1–2 ms) with no overshoot during high voltage retrace. MCP detectors were matched for bias current and selected for low background rates and gain uniformity. After sensor assembly, calibrations were performed in high vacuum ($< 10^{-6}$ Torr) and included background noise sensitivity, MCP background rates, MCP pulse height distribution tests, energy-angle characterization, analyzer concentricity tests, relative sensitivity characterization, and sweep mode testing.

MCP tests within the analyzer assembly showed background rates 10 to 100 times higher then those observed during subassembly testing with MCPs exposed to the chamber. After several subsystem and system level checks, it was recognized that the higher background resulted from higher pressure at the MCPs which were buried deep in a newly assembled instrument. Internal instrument out gassing, and its associated higher pressure, was the source of higher background rates. By allowing more time in high vacuum prior to testing, and by scrubbing the MCPs prior to the beginning of calibration testing, background rates were reduced to relatively low levels that did not impact calibrations. Similar high background rates were observed on some sensors during thermal vacuum testing at the spacecraft level at UCB, with background seen to correlate with chamber pressure and to decrease with time. Spacecraft level Integration and Test (I&T) at JPL, with higher vacuum during the HV tests, showed expected background rates of $\sim 1/\mathrm{s\,cm}^2$. In-flight data have similarly low background rates.

Figure 7 shows the energy-angle calibration for the electron sensor on THC. The inner hemisphere voltage is kept constant while the beam energy and "out-of-plane" alpha angle are varied. The average of this response over alpha angle provides a characteristic energy curve and determines the analyzer energy constant (average energy divided by hemisphere voltage). When the response is averaged over energy, the test provides a measure of the out-

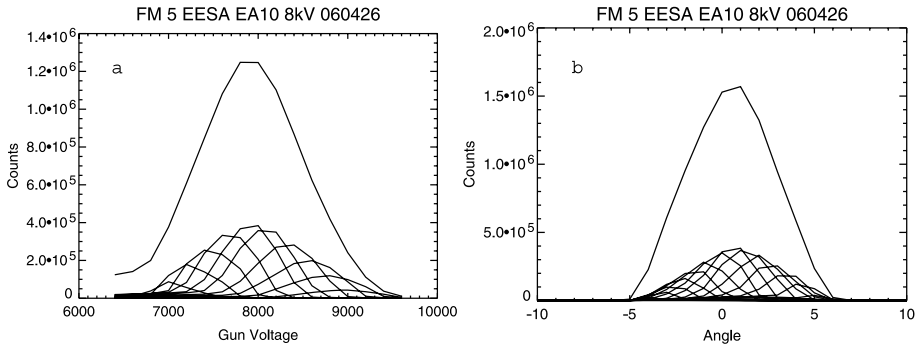

Fig. 7 (**a**) Average energy response and (**b**) average "out of plane" alpha angle response of the THEMIS electron ESA. The *lower curves* are energy (angle) response at a single angle (energy). The analyzer energy constant is determined from the *curve on the left*

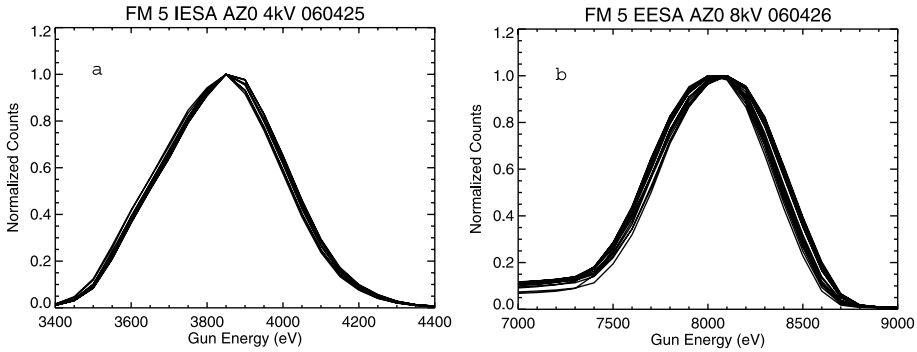

Fig. 8 Energy response curve at 0° alpha angle for the beam at 15° increments around the 180° field of view for ions (**a**) and electrons (**b**). Variations between curves indicate about 1% variation in the analyzer energy constant with look direction

of-plane angular acceptance of the instrument. These tests were compared with simulations to confirm proper analyzer operation. Energy-angle tests are performed at three different rotation angles and the instrument's energy calibration is determined from the average energy constant. No significant differences in the energy constant with look direction were found.

One of the most important tests performed was for concentricity of the analyzer's hemispheres. If the hemispheres are not concentric, the energy of measured particles will be a function of its 180° FOV, which will complicate data analysis and in-flight calibrations. Although the energy-angle test described above can often identify hemisphere misalignment, a faster test uses a single alpha angle for the beam and sweeps the beam energy at a dozen different look directions. Figure 8 shows examples of analyzer concentricity tests for the electron and ion sensors on THC. All THEMIS ESAs were found to have good concentricity with about 1% or less variation in energy with look direction. This accuracy corresponds to a misalignment of hemispheres of $\sim$15 μm.

Figure 9 shows results from relative sensitivity tests performed on the THEMIS ESAs. For this test the sensor and the beam are optimized for beam throughput and the analyzer is rotated about the symmetry axis. For a parallel beam, the response should be roughly

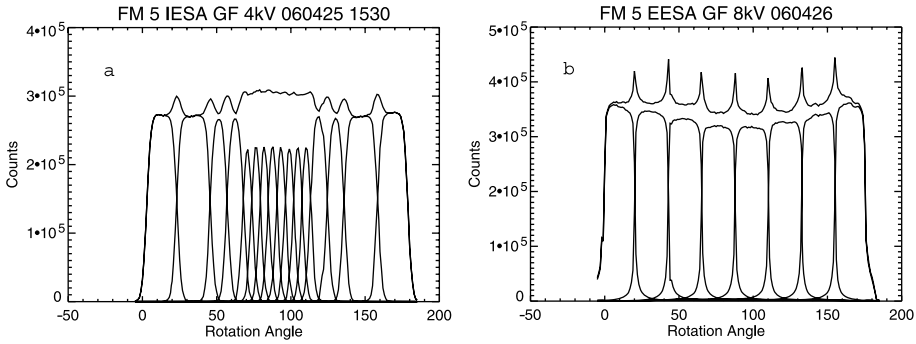

Fig. 9 Azimuthal response of the ion (**a**) and electron (**b**) sensors on THC to a parallel beam at 0° alpha angle reveal the 16 anode and 8 anode patterns for the two sensors. A small amount of particle double counting can be seen as enhanced response at the borders between anodes

flat, with deviations revealing any large asymmetry in the assembly. The ∼10% variations in response with look direction are normal and result from a combination of MCP detector bias angle (Gao et al. 1984) and double counting of events at anode boundaries. This test was used early in the THEMIS calibrations to identify a problem with an aperture opening mechanism. A ∼40% variation in sensitivity with rotation was observed on two sensors that simultaneously showed little variation in concentricity. This indicated the top-hat was not seating properly. Careful examination with backlighting revealed the seating problem which was barely visible to the eye. A clearance problem was identified and the problem was fixed on all sensors. Although these tests provide a preliminary estimate of the uniformity of response, relative sensitivity is more accurately quantified during in-flight calibrations discussed in Sect. 2.4.

Additional ground calibrations were performed to assure proper operation of the sensor in flight configuration. These included tests of nominal sweeping modes with a beam source and full spacecraft level testing of flight data packaging. Absolute sensitivity of the sensors and relative efficiency of the detectors with energy were not calibrated due to lack a beam monitor. However, the electron and ion count rates were very similar for different instruments with the same beam settings and same instrument geometry providing confidence that beam fluxes were stable over time and that the different sensors were nearly identical. Since an instrument's absolute efficiency will change on orbit as its detectors age, in-flight calibration procedures are required to determine absolute and relative calibrations. These tests are discussed in Sects. 2.2, 2.5 and 2.6.

2 In-flight ESA Calibrations

The THEMIS and Cluster missions are the only multi-spacecraft missions in which four or more satellites have been kept in close proximity, allowing detailed cross-calibration efforts between instruments. Unlike the Cluster mission where the electron and ion plasma measurements originated from separate groups and where data products differed in both time and angular resolution, THEMIS offers the advantage of having all the plasma measurements available with the same resolution and format. Furthermore, since all the THEMIS data are distributed as a single data set, spacecraft potential (Bonnell et al. 2008) and magnetic field (Auster et al. 2008) measurements are instantly available in raw or processed form for use in

the cross-calibration efforts. This advantage has allowed a detailed cross-calibration effort to be performed in a rather short period of a few months early in the mission. Lessons learned from this effort should be useful for future multi-satellite missions.

The in-flight calibration of the THEMIS electron and ion plasma instruments required inputs from several other instruments including spacecraft potential measurements supplied by EFI, magnetic field measurements supplied by FGM, and spacecraft attitude and timing information supplied by the Mission Operations Center at Berkeley. These inputs were crucial for proper interpretation of the measurements and for confirmation that the sensor operation was nominal. In addition, ESA data were used for in-flight calibration of the EFI and SST instruments as described by Bonnell et al. (2008) and Larson et al. (2008), respectively.

The following sections describe the methodology used for the ESA in-flight calibrations, along with the basic rational for each analysis. Part of this process was the identification of data collection times where known properties of the plasma, such as charge neutrality and gyrotropy, could be used to identify small variations in the sensor response. In addition, the absolute sensitivity calibrations required the use of solar wind data from the Wind spacecraft. During this calibration effort, unexpected variations in the ratio Ni/Ne were discovered for several orbits. This led to an investigation of sensor efficiency as a function of energy and the discovery of an unexpected small variation in analyzer sensitivity due to leakage fields through the analyzer's exit grids. Lastly, the THEMIS ESA calibration effort is not a one-time process. Maintaining accurate calibrations will require continuous monitoring of the detector gain with regular bias voltage adjustments, along with repeated iterations of the techniques described below.

2.1 Spacecraft Potential Corrections

In order to cross-calibrate plasma sensors using density as a measure of sensitivity, one must include corrections for spacecraft charging (Pederson et al. 1998). This is especially important for the electron density calculation where inclusion of spacecraft photoelectrons can result in large errors to the density. The electric field experiment (Bonnell et al. 2008) provides a proxy for the spacecraft-to-plasma potential by measuring the potential of Langmuir sensors relative to the spacecraft. With a proper bias current to the Langmuir sensors (roughly 25% to 50% of the sensor photoemission current) these sensors should float within about a volt of the "local" plasma potential. There are several caveats here. First, the Langmuir sensor and spacecraft must be in sunlight to obtain good current balance between photoemission and plasma collection. Second, by "local" potential, we mean local plasma potential adjacent to the Langmuir sensor. This potential differs from the plasma potential we wish to use as a reference for the spacecraft since the spacecraft, the antenna, and their photoelectrons all perturb the "local" plasma environment. To account for this difference, we introduce a potential "scale factor" that corrects the measured "local" potential to actual plasma potential at large distances from the spacecraft. This "scale factor" is a function of spacecraft potential (or plasma and photoelectron distributions), complicating the calculation. Third, the difference potential between the Langmuir sensor and "local" plasma can vary from near zero in high density plasmas to about two volts in low density plasmas. This potential "offset" also depends on bias current applied to the Langmuir sensor. So, like the "scale factor", the "offset" potential varies with spacecraft potential (or with plasma and photoelectron distributions). Therefore, calculating the spacecraft potential to be applied to a particle distribution is non-trivial since the measured Langmuir-sensor-to-spacecraft potential must be corrected for changing parameters, such as Langmuir sensor bias current and the plasma distribution.

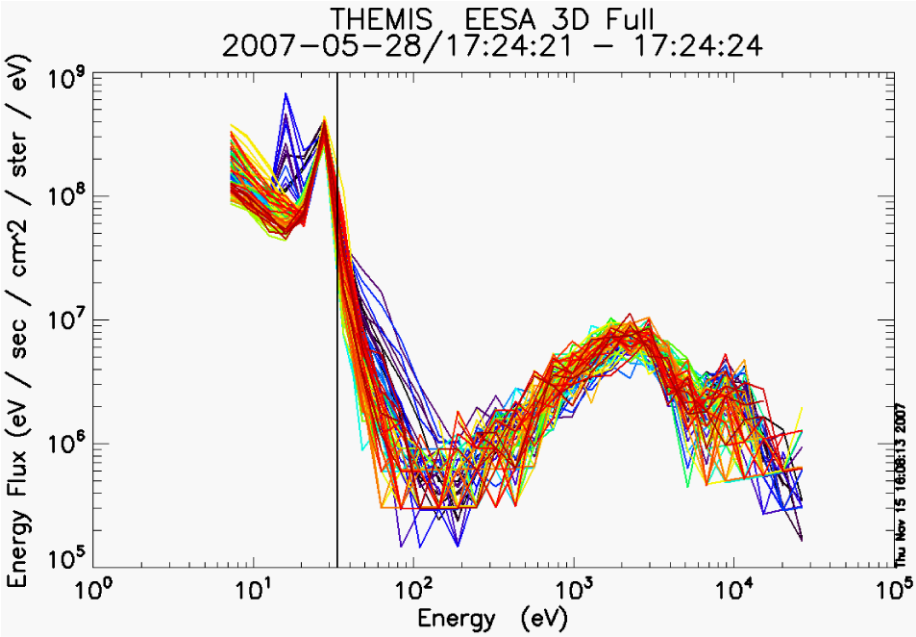

Fig. 10 Electron spectra from THC in a low density ($n_e \sim 0.2$) magnetospheric plasma. Each of the 88 solid angle bins are plotted separately. The line indicates the inferred spacecraft potential using (1). The peaks at 15 eV and 28 eV are due photoelectrons emitted from the axial and radial Langmuir sensors, respectively. Spacecraft photoelectrons dominate most solid angle bins below 21 eV. Field-aligned electrons are resolved between 40 eV and 150 eV (*blue-black*), and isotropic hot plasma is observed at higher energies

For THEMIS, the spacecraft potential, Φ_{sc}, is estimated with the following equation.

$$\Phi_{sc} = -A(\Phi_{sensor} + \Phi_{offset}) \tag{1}$$

where A is a near unity "scale factor", Φ_{sensor} is the average radial Langmuir-sensor-to-spacecraft potential, and Φ_{offset} is the potential "offset" discussed above. Axial Langmuir sensors are not used in the estimate. Current software sets Φ_{sensor} to the spin-averaged potential of two or four radial Langmuir sensors, and treats A and Φ_{offset} as constants over an interval with default values of $A = 1.15$ and $\Phi_{offset} = 1.0$ V, respectively. These values were determined empirically from spacecraft THC early in the calibration effort by comparisons of calculated electron and ion densities as a function of A and Φ_{offset}. This choice of parameters generally prevents spacecraft photoelectrons from being included in the electron density calculations. Both numbers are consistent with those estimated from previous missions (F. Mozer private communication) and from THEMIS EFI modeling (C. Cully private communication).

The need for a "scaling factor" is illustrated in Fig. 10. The two electron peaks at 15 eV and 28 eV are the result of photoelectrons emitted from the axial and radial Langmuir sensors, respectively. The vertical line indicates the spacecraft potential determined from (1) using the default values for the scale factor and offset. If no scaling factor were needed, the proximity of the spacecraft would not matter and both peaks would be at the same value. However, at the $\sim$2 m distance of the axial Langmuir sensors, the local plasma potential is about half the spacecraft potential relative to the distant plasma. Since the axial Langmuir

sensor comes to equilibrium with the local plasma, its photoelectrons only gain $\sim 0.5e\Phi_{sc}$ before reaching the plasma sensor. In contrast, the plasma near the radial Langmuir sensors (~ 20 and ~ 24 m distance) is at a potential much closer to the distant plasma potential resulting in a spectral peak that is much closer to the actual plasma potential.

In plasma regimes where the bulk of the electrons and ions have energies larger than $e\Phi_{sc}$, plasma moment calculations are not be very sensitive to small errors in the estimated Φ_{sc} as long as Φ_{sc} is large enough to eliminate spacecraft photoelectrons. However, within the magnetosphere there is often a cold electron component with a sizeable density. This is especially true within the plasmasphere or within plasmaspheric plumes where cold plasma dominates. These cold electrons appear at energies $\sim e\Phi_{sc}$ and are difficult to separate from spacecraft or Langmuir sensor photoelectrons. In addition, these cold electrons reduce the Debye length, resulting in "scale factors" close to one and Langmuir sensors that float very close to plasma potential. For THEMIS data, which generally have energy bins such that $\Delta E/E \sim 0.32$, it may be impossible to separate these cold plasma electrons from the Langmuir sensor photoelectrons. Data with these problems were avoided during the in-flight calibration effort.

THA and THB spacecraft did not have Langmuir sensors deployed during the first eight months of the mission and therefore made no in situ potential measurements. To perform cross-calibrations of plasma sensors between spacecraft, it was essential to correct for spacecraft charging. Therefore we developed an empirical method to estimate the spacecraft potential on THA and THB based on the potential of the near by THD. It was not sufficient to assume the same potential as THD since the bias currents applied to the Langmuir sensors have a significant affect on spacecraft potential. To develop an empirical relationship between spacecraft, we used data from the EFI bias sweeps (Bonnell et al. 2008) to estimate the change of spacecraft potential as a pair of Langmuir sensors were cycled on/off. A perpendicular Langmuir sensor pair was then used to measure the change in spacecraft potential. The measurements showed a linear relationship between spacecraft potential with and without bias current applied.

$$\Phi_{\text{no-bias}} = 0.7\Phi_{\text{bias}} + 0.5, \tag{2}$$

where Φ_{bias} and $\Phi_{\text{no-bias}}$ are difference potentials between the spacecraft and a perpendicular Langmuir sensor pair in volts, with bias current to a radial Langmuir sensor pair cycled on and off, respectively. In addition, the axial-booms were found to produce a ~ 0.3 V shift in spacecraft potential. Not enough samples were obtained to determine any dependence of this shift on Φ_{bias}. Combining the above measured differences with (1), we estimated the spacecraft-to-plasma potential on THA and THB as

$$\Phi_{\text{THA}} = \Phi_{\text{THB}} = 0.49\Phi_{\text{THD}} + 1.22, \tag{3}$$

where Φ_{THD} is determined from (1).

The above estimated potentials were used for some of intervals in the cross calibration effort described in Sect. 2.5. However, the EFI operating voltages on the usher and guard surfaces (see Bonnell et al. 2008 for the antenna geometry) were changed from -8 V to $+4$ V relative to the Langmuir sensor surface on June 22, 2007. This reduced spacecraft charging and changed the 0.49 scale factor determined above. To recover an equivalent formula to (3), we performed empirical comparisons between electron spectra and calculated densities, varying the scaling factor to get the best agreement. These comparisons resulted in (4) which should be valid between June 23 and September 10, 2007.

$$\Phi_{\text{THA}} = \Phi_{\text{THB}} = 0.8\Phi_{\text{THD}}, \tag{4}$$

For most of the in-flight calibration effort discussed below, we selected periods where errors in our estimated spacecraft potential would have minimal effect on the calibration result. During the course of this effort, we observed additional aspects of the dependence of spacecraft potential on the plasma that were not included in this in-flight calibration but are worth noting for future data analysis efforts. First, the Langmuir sensor-to-spacecraft potentials on different "identical" spacecraft in the same environment were not identical and could differ by ∼5% at potentials of ∼ 6–8 V. Smaller differences were observed at lower potentials. Although this error is not large, it could cause ∼5% difference in estimated electron plasma density in the solar wind. Second, the ratio of potentials on different spacecraft as the environment changed was not a constant, indicating this was not just a simple difference in a constant "scale factor". These results indicate that for very precise estimates of density, (1) will require a different "scale factor" and "offset potential" for each spacecraft and that these parameters likely have a weak functional dependence on potential. For missions such as MMS, where resolving small differences between spacecraft is essential, in-flight calibration efforts must be planned to quantify these small differences.

2.2 Energy-Dependent Efficiency Corrections

Microchannel plate (MCP) detectors are known to vary in efficiency with the incident particle energy (Goruganthu and Wilson 1984; Straub et al. 1999) and with the incident particle angle relative to the microchannel bias angle (Gao et al. 1984). For THEMIS ESAs, the bias angle of the plates was oriented so that average variations of incident angle around the MCPs was minimized, and any bias angle efficiency variations are included in "relative efficiency calibration with look direction" discussed later. For energy dependent efficiencies, we initially adopted values published in the literature for electron and ions as shown in Fig. 11a and 11b.

However, early in the calibration effort it was discovered that the calculated ratio of electron and ion density appeared to depend upon ion energy. In particular the presence of low energy (< 100 eV) ions seemed to increase the Ni/Ne ratio. Not knowing the source of this energy-dependent efficiency change, an empirical approach was adopted, testing various energy-dependent changes to the ion efficiency to determine the approximate variation required to improve the Ni/Ne ratio. These comparisons indicated the ion sensor was significantly (> 40%) more efficient at low energies (<100 eV) than at higher energies (>500 eV). Since ions are pre-accelerated to ∼2 keV before striking the MCP, it is unlikely that small variations in initial energy could cause large changes in detector efficiency. Instead we realized that the efficiency change must stem from leakage fields into the electrostatic analyzer

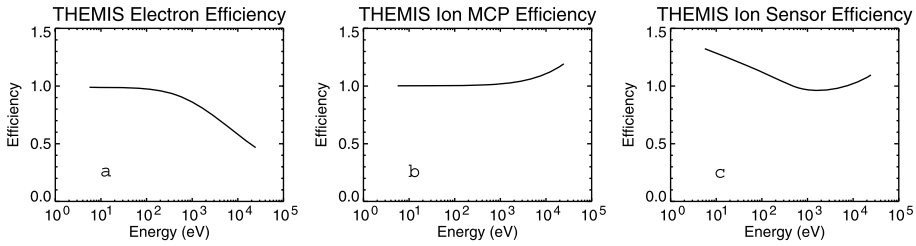

Fig. 11 (**a**) Electron MCP energy efficiency adapted from (Goruganthu and Wilson 1984), (**b**) ion MCP energy efficiency adapted from Funsten (private communication), and (**c**) ion sensor energy efficiency (analyzer+MCP) which includes leakage fields at the exit grids that increase analyzer geometric factor over the ideal analyzer. See text for discussion

from the −2 kV bias voltage on the front of the MCPs. Analyzer simulations had ignored this effect because an exit grid was used to shield the inside of the analyzer.

To quantify the effects of the leakage fields, we used a combination of analyzer simulations and grid transparency corrections. First, a 3-D model of the exit grid and nearby surfaces showed that 2–3% of the MCP bias voltage would penetrate the grid. Second, the impact of this leakage field was characterized with a 2-D analyzer simulation by replacing the "ideal" exit grid with a potential surface that varied linearly from 40 V at the edges to 60 V at the center. The analyzer geometric factor was found to increase by ∼30% at low energies due to this leakage field, with an e-fold drop in this additional sensitivity at ∼180 eV. Third, we recognized that a secondary effect of the leakage field would be to focus low energy ions away from the grid wires, increasing the 90% exit grid transmission to about 100% at low energy. This was also simulated to estimate the exit grid effective transmission as a function of energy. Fourth, a separate "MCP grid" was placed in front of the detector and biased at the MCP voltage to increase detector efficiency. Due to the alignment of the MCP grid with the exit grid, the transmission of the MCP grid could also vary with energy. Simulations showed a complicated transmission function for the MCP grid caused by particle focusing by the exit grid, with some increased transmission at lower energies. Full characterization of this dependence was not attempted and instead an increase from 90% to 95% at low energies was estimated from the simulations. Combining these leakage field effects we obtained a ∼45% increase in analyzer geometric factor at low energies. Figure 11c shows the final energy-dependent efficiency correction used for THEMIS ion ESAs, which includes both the leakage field and the MCP detector variations (see Fig. 11b).

We point out that a similar energy-dependent analyzer affect is likely present in the electron analyzers. It would manifest itself at lower energies since the voltage on the front of the MCPs is only ∼450 V. Based on ion sensor simulations, we might expect the enhanced sensitivity to have an e-folding decrease at ∼45 eV from the maximum transmission at ∼0 eV. In addition, there is a second effect exclusive to electron analyzers. Electrons at energies >50 eV are capable of producing secondary electrons when they strike the outer or inner hemisphere. These low energy secondary electrons will be accelerated to the detector by the leakage fields if the incident particle strikes the hemisphere near the analyzer exit. This additional enhancement in analyzer secondary production kicks in at about the same energy that the enhanced throughput falls off. If the effects are similar in magnitude, it may be that the combined response is relatively flat. To sort out these effects would require a complex analyzer simulation which is beyond current THEMIS data analysis plans. However, after many comparisons between ion and electron densities, we conclude there are no large changes in the electron sensor (detector+analyzer) energy efficiency curve at these energies indicating the combination of these two effects has a relatively flat dependence on energy. Therefore the energy efficiency curve shown in Fig. 11a was adopted and any energy-dependent sensitivity changes due to leakage fields are assume to be absorbed in the overall geometric factor of the electron sensors.

2.3 Instrument Dead Time Corrections

Corrections for instrument dead-time can be important in regions of high particle count rates such as a high-density magnetosheath. For plasma sensors, lost counts due to instrument dead-time result from a combination of electronic and detector dead-time. For THEMIS, electronic dead-time was measured as part of the calibration and determined to be 170 ± 10 ns for all Amptek A121 preamplifiers. Detector dead-time is more difficult to determine. For microchannel plate detectors (MCPs), the dead-time is caused by a decrease in gain at

high count rate that results in some events dropping below the preamplifier threshold. The gain drop occurs when the microchannels are unable to completely replenish the charge lost after the previous firing. THEMIS ESAs were fitted with high current MCPs for fast recharging. "Back of the envelope" estimates of the detector dead time, assuming a 6 MHz broad angle flux that illuminates a 22.5° anode, suggest the effective detector dead time is only ∼30 ns at this high rate. The calculation assumes the signal current is limited to 10% of the fractional MCP strip current for the anode (∼4 μA), and that the detector pulse height distribution maintains a Gaussian shape with a FWHM equal to its peak. Since the estimated detector dead time is much smaller than the preamplifier dead time, detector dead-time is not expected to be important unless the particle flux manifests as an intense narrow beam that is focused on a small portion of the detector. The software assumes a nominal 170 ns dead-time for all detector-preamp combinations.

Nature allowed in-flight testing of our dead-time correction. Figure 12 shows ion and electron data collected during a period of high density magnetosheath plasma. The top panels show ion and electron spectrograms, while panel c shows the uncorrected ion and electron densities and panel d the ratio of these densities. The electrons require significant dead time corrections prior to 18:30 UT, resulting in a density ratio that exceeds one. Panels e and f show the dead-time corrected densities with an expected ratio of about 0.9 during this period, confirming that the preamplifier dead time correction accounts for the majority of high rate dead time correction. While interpreting this plot, the reader should ignore the period with un-shocked solar wind (19:30–21:20 UT) where ion densities are underestimated in 32 sweep/spin mode.

2.4 Calibration of Relative Efficiency with Look Direction

Themis ion and electron ESAs have 16 and 8 discrete anodes, respectively, each of which requires a "relative efficiency" calibration factor to account for small variations in sensitivity with look direction. These relative efficiency corrections are approximately unity and do not reflect changes in overall instrument sensitivity. Overall instrument sensitivity is accounted for in the "absolution efficiency" calibration factor discussed in the next section.

For THEMIS electron sensors, the "relative efficiencies" correspond directly to the eight 22.5° anodes that cover 180° of polar angle. For ion sensors, which have 16 anodes and up to 5.6° resolution, an ideal relative efficiency calibration would result in 16 efficiency values. However, THEMIS data collected in regions useful for calibrations only maintain 22.5° resolution. Therefore ion relative efficiencies are determined in the same manner as those for electrons. Anodes within a 22.5° sector are assumed to have the same relative efficiency as the sector.

THEMIS relative calibrations were accomplished by finding data intervals inside the magnetosphere that met the following criteria:

1. Flows determined by the ion sensor must be small (< 30 km/s) and random. This allows us treat the raw data as if it is collected in the plasma frame and ignore pitch angle asymmetries caused by flows.
2. The magnetic field must be relatively constant and make a significant angle ($> 20°$) with the spin axis. This assures that the same pitch angle is measured by more than one anode during a spacecraft rotation.
3. The average pitch angle distribution of 1–20 keV plasma must be relatively smooth and vary by no more than a factor of 3 (no large anisotropies). This allows us to use a small number of polynomials in the fit and avoid high order terms that tend to be affected by statistical fluctuations or beams much narrower than the angle bins. The high energy range (> 1 keV) is selected so spacecraft potential variations are unimportant.

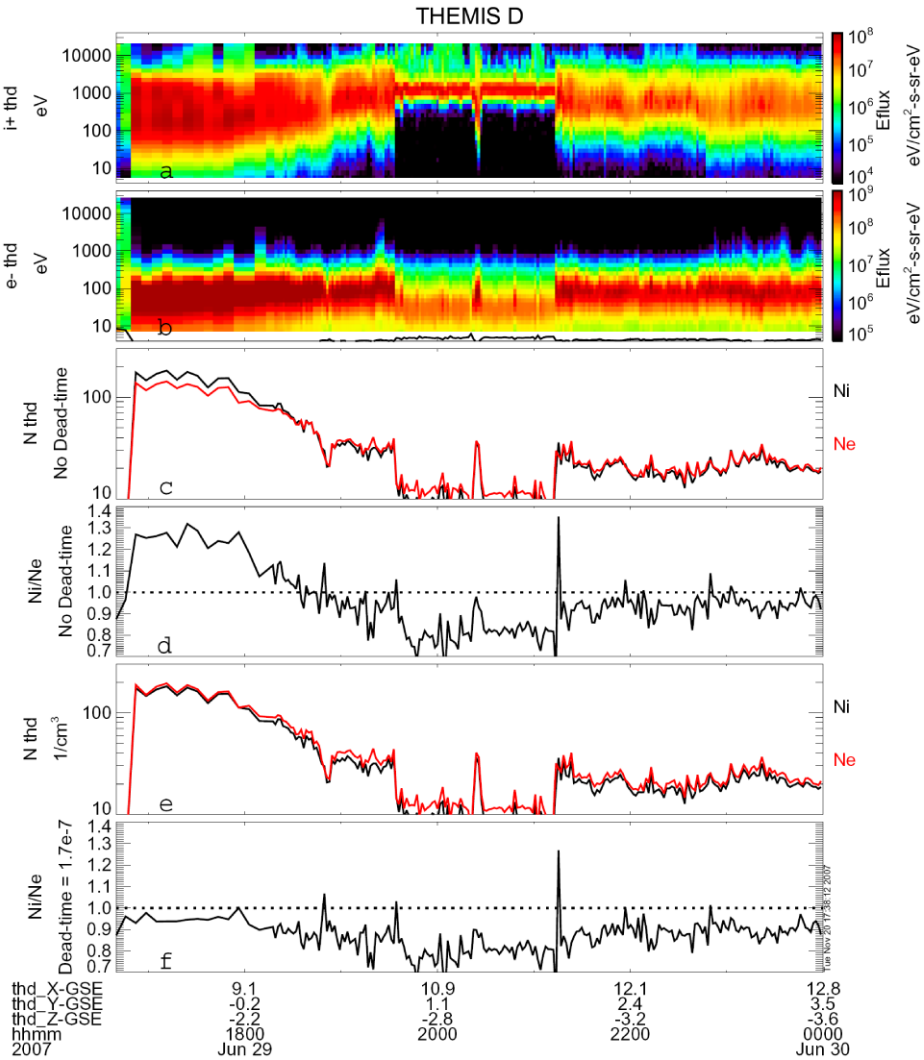

Fig. 12 The plot illustrates the importance of dead-time corrections during a day with high magnetosheath density (<19:00 UT). *Top panels* are ion (panel **a**) and electron (panel **b**) spectrograms. Panel **c** shows the ion (*black*) and electron (*red*) densities uncorrected for dead-time, and panel **d** illustrates how the ratio of these densities results in unphysical 1.0–1.3 values due to underestimation of the electron density. Density ratios should be ∼0.9 since solar wind alpha content causes an underestimation of ion density (the calculation assumes protons only). Panel **e** shows the dead-time corrected densities have good agreement and panel **f** illustrates density ratios of ∼0.9 as expected. In addition, within the solar wind (19:30–21:20 UT) the ion density is further underestimated due to the narrow beam width

4. Data intervals must contain 1–2 hours of Fast Survey data. This criterion assures that 40–75 spins of high angle resolution (88 solid angles) data are available for the fit.

Data between May 31 and August 13 were examined for these criteria, and 10 to 20 intervals were found for each spacecraft. Data from each interval was averaged, sorted by pitch angle, and fit to a 6th order symmetric polynomial $f = a + bx^2 + cx^4 + dx^6$, where

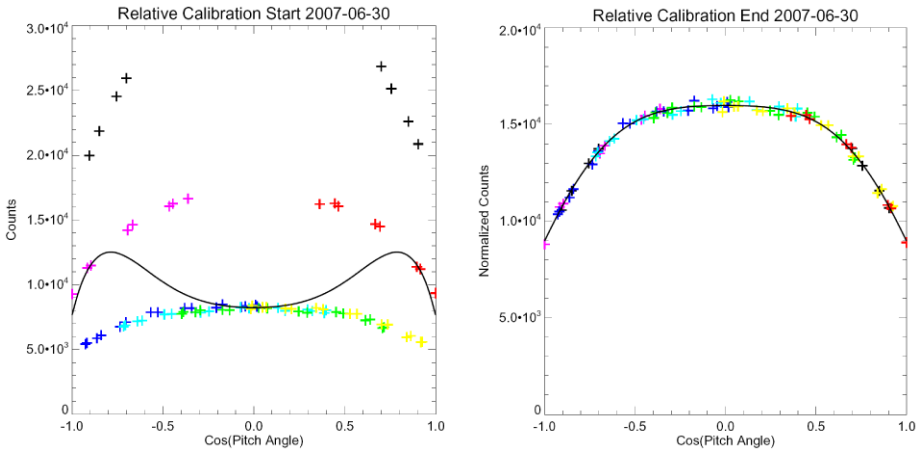

Fig. 13 Plots generated as part of the relative anode efficiency calibration algorithm. Different anodes are different colors and each "+" represents a different solid angle bin. (**a**) The *left plot* shows the raw counts in each solid angle bin as a function of pitch angle. *Black* colored bins have 4 times the counter accumulation time and *red/magenta* bins have twice the accumulation time of the other bins, accounting for the initial large variations. (**b**) The *right plot* shows normalized counts after anode efficiencies have been applied. The variation in normalized counts (9×10^3 to 1.6×10^4) is due to actual pitch angle anisotropy. Anode efficiencies are determined through minimum variance to a 6th order symmetric polynomial. The initial and final best fit polynomials are the *solid lines* in each plot. Different anodes had relative efficiencies within 10% of unity

$x = \cos\theta$ and θ is the pitch angle. Relative efficiencies were calculated by minimizing the variance in the least-squares fit and the fitting algorithm was repeated. This procedure was iterated until efficiency estimates converged to optimal values for each interval. Figure 13 illustrates the initial and final pitch angle distributions, with different anodes indicated by color and each point a different solid angle. After convergence to the right plot in the figure, the combined anode efficiencies and integration time effects are determined. Two anodes (red, magenta) have twice the integration time and two anodes (black) have four times the integration time, which accounts for the majority of the initial difference in the left plot.

Once efficiencies were calculated for the different intervals, they were averaged and incorporated into the code. Anode efficiencies were generally within about 10% of unity, with the largest variations associated with slightly smaller anodes in the pole channels (which were designed to prevent noise counts near the edge of the microchannel plate detectors). The standard deviation of the relative efficiencies over the intervals was $\sim 1.5\%$ for ions and $\sim 1\%$ for electrons indicating sound methodology and high precision. Since there were no systematic trends in these efficiency variations with time, we assume that these relative efficiencies are constant.

In using a symmetric polynomial to model the pitch angle distribution, we assumed that the distribution was stable and that sufficient bounce-averaging of plasma between magnetic poles had removed any asymmetry in the distribution. This is probably not the case and therefore this assumption may introduce an asymmetric, systematic error to the relative efficiencies. This asymmetry cannot be removed by simply including asymmetric terms in the pitch angle model. This is because the pitch angle overlap between anodes is generally limited to adjacent anodes so the fitting algorithm does not have a strong constraint on large-angle variations. Any large-angle asymmetry in the input distribution cannot be distinguished from an asymmetry in efficiencies. Therefore we are forced to use other methods to evaluate and correct for asymmetries in the response.

A simple estimate of the magnitude of any asymmetric response can be made by comparing the sensitivity of the two halves of the sensor. Since the sensors are symmetric, with hemispheric concentricity generally better than 1%, the average response of the 0° to 90° and 0° to −90° sensor halves are expected be very close. Indeed they are found to differ by only ∼0.5% for electrons, and by <2% for ions (except for one sensor that differed by ∼4%). Ion distributions during quiet periods in the magnetosphere were then checked for systematic flows in the z-direction and no statistically significant flows were found. Since small errors in electron ESA asymmetry can result in large flow errors along the spacecraft spin axis, we compared electron and ion flows in the magnetosheath during July 21–25, 2007. A first order ($\cos\theta$) asymmetry at the 1–3% level was then introduced to the electron efficiencies to obtain agreement between ion and electron flows. This correction was then tested for data from August 21–25, 2007 and found to provide consistent spin axis velocities between ions and electrons.

2.5 Cross-Calibration of the Sensors

The five electron and five ion ESAs on the THEMIS spacecraft each require a "sensor-level relative efficiency" calibration that accounts for overall variations in efficiency between instruments. These "near unity" efficiencies will change with time as detectors age and as detector bias voltages are increased to compensate for decreasing detector gains. We chose to separate this relative cross-calibration from an absolute calibration since we had all five satellite data sets in close proximity at the start of the mission and because we lacked a reference for absolute calibration. Since THEMIS does not have a high-frequency measurement of the plasma frequency, absolute calibration will require comparisons with upstream solar wind monitors, such as Wind or ACE, as discussed in the next section.

For this cross-calibration we used the already-determined relative anode efficiencies and energy-dependent detector efficiencies to calculate a sensor-level calibration factor that forces agreement between the separately determined densities. These calibrations cannot be performed in the magnetosphere since it often contains significant cold plasma that is unmeasured. Instead we focused on the magnetosheath where flows were large enough to assure nearly all ions were measured and where spacecraft potential corrections were relatively small. We emphasize that even though the spacecraft potential in the magnetosheath is rather low, typically 5–6 volts, inclusion of the spacecraft potential in the density calculation is critical. For spacecraft whose electric field sensors were not deployed (THA and THB), we used measured potentials from other spacecraft, with corrections as described in Sect. 2.1. Lastly, since the ion plasma sensor is not mass resolving, we must also account for differences in estimated density between ion and electron sensors due to the presence of alpha particles in the solar wind. These were accounted for by using upstream solar wind measurements from the Wind spacecraft.

Since THC was the first spacecraft with deployed electric field sensors, early cross-calibration efforts focused on inter-comparisons of its electron and ion sensors. Its observations were used to investigate two months of data (late-May to early-August, 2007) and select ten days where cross-calibrations would be possible. Selected days had measurements from all spacecraft while in the magnetosheath, and if possible were selected for low alpha content to minimize mass-dependent corrections. Since these are relative calibrations, the electron sensor on THC on June 28, 2007, was selected as a reference, its pre-launch estimated geometric factor used as a baseline, and its efficiency set to one. THC's ion sensor was then cross-calibrated, and its pre-launch geometric factor adjusted to give the same density as the electrons, and its efficiency was set to one. Following these baseline determinations, we set the geometric factors of all other electron and ion sensors to the same values

determined above and calculated their sensor-level efficiencies to get agreement between densities. This was accomplished by first cross-calibrating ion and electron sensors on each spacecraft, then cross calibrating electron sensors on each spacecraft with THC's electron sensor.

Figure 14 shows an example of the type of data used to perform the cross-calibration. The top four panels are ion and electron spectrograms and allow quick determination of the various regions: magnetosphere (<12:30 UT), magnetosheath (12:30–17:00 UT) and solar wind (>18:00 UT). Panel e shows the density determined from the electron and ion sensors on THC and THD, after the calibration process. As discussed above, ion–electron sensor cross-calibrations on the same spacecraft are performed in the magnetosheath. Panels f and g show that the Ni/Ne ratios have been matched to $\sim$0.99 during the 12:30–17:00 UT period. (Upstream Wind-3dp plasma data indicated very low alpha content.) The inter-spacecraft cross-calibration is performed between electron sensors in the solar wind (>18:00 UT) as illustrated in panel h. The variance in the plots results from a combination of counting statistics and temporal variations less than the spin period.

The above calibration procedure was repeated for the 10 selected days. It was then assumed that relative efficiencies of sensors only decreased with time as the detectors aged unless detector bias voltage was increased. This assumption forced a renormalization of the sensor-level efficiencies on each day, except our reference day of June 28, so that each sensor's efficiency monotonically decreased in time. Over the 72 day interval starting 2 months after sensor turn-on, sensor efficiency degradation of 5% to 11% was estimated by this method. Table 2 shows the initial (07-05-15) and final (07-08-25) values for relative efficiency for the 10 sensors illustrating the variations in their loss of sensitivity. Sensor geometric factors can be calculated by combining the geometric factor from Table 1 with the relative sensitivity in Table 2 and the energy dependent efficiency in Fig. 11. In addition, the MCP detector voltage was raised on three of the sensors toward the end of this interval, with no measurable impact on detector efficiency. This suggests the drop in sensitivity may not be a detector gain issue but rather a front-end particle detection efficiency change. In any case, sensitivity degradation is assumed to come from MCP scrubbing, which is expected to stabilize after a few months of high counting in the magnetosheath. Since random errors in the determination of these detector efficiencies may result in an over estimation of this degradation, it may be necessary to correct these calibrations with an overall mission-level efficiency using upstream solar wind measurements.

We close this section by pointing out that the ESA MCP detectors are tested each month for gain to assure that the peak in their pulse height distribution is about a factor 8 above preamplifier threshold (see Sect. 1.1). During 16 months of operations, four of the five electron sensors, and three of the five ion sensors, have had their MCP voltage increased one or more times to maintain this gain. No noticeable change in sensitivity was observed during any of these increases indicating they were performed well before a significant number of events dropped below preamplifier threshold. It is not known whether the drop in efficiency discussed above was due to front-end changes in incident particle secondary electron production, or due to changes in gain that result in the loss of events below threshold. Continued monitoring and comparison of instrument sensitivity should provide information on MCP degradation and longevity. Lastly, absolute calibrations, described in the following section, should provide additional information to track long term changes in sensitivity.

2.6 Absolute Calibrations

The calibration efforts described above resulted in a consistent set of relative calibrations between measurements within a sensor, and consistent measurements between different

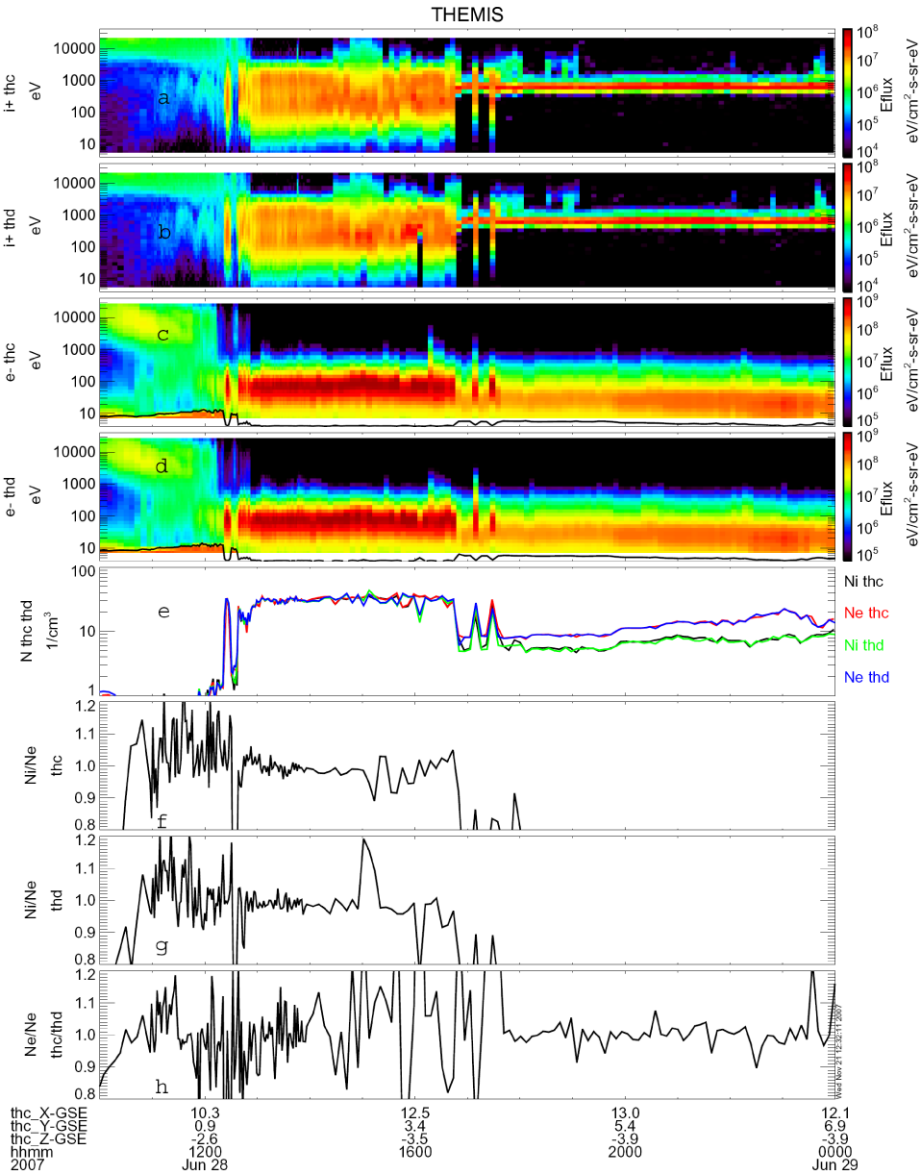

Fig. 14 Example of the cross-calibration analysis. Ion–electron sensor cross-calibrations use Ni/Ne ratios measured on the same spacecraft (panel **f**, **g**) within the magnetosheath (12:30–17:00) and match the result to the expected ratio based on upstream alpha content, ∼0.99 in this case. Inter-spacecraft cross-calibrations match electron densities within the solar wind (>18:00 UT) as illustrated in panel **h**. Solar wind ion densities are underestimated due to the narrow solar wind beam and therefore not used in calibrations

sensors. However, there was no test in the above procedures that determined the absolute sensitivity of the sensors. All measurements of the even moments, such as density and pressure, or measurements of flux and energy flux, which are proportional to density, were likely incorrect by some scale factor. For these initial calibrations, the absolute sensitivity, or ab-

Table 2 Relative sensor efficiency

Spacecraft	eESA 07-05-15	eESA 07-08-25	iESA 07-05-15	iESA 07-08-25
THA	1.010	0.935	1.075	1.010
THB	1.000	0.890	1.100	1.050
THC	1.030	0.910	0.995	0.920
THD	0.945	0.845	1.015	0.970
THE	0.865	0.805	1.085	1.035

solute geometric factor, was estimated from the electron analyzer simulation combined with expected losses from an exit grid and an estimated 70% MCP detection efficiency. To determine the absolute calibration requires a comparison of the THEMIS ESA response to a known "standard candle" plasma parameter. Generally this standard candle is the plasma frequency which determines the electron density. However since THEMIS spacecraft do not have high frequency wave receivers, absolute calibration has to be determined through comparisons with other spacecraft. Since the THEMIS spacecraft are rarely near any other magnetospheric spacecraft for cross-calibrations and since magnetospheric plasma regimes vary dramatically in density and pressure, the most favorable location for consistent cross-calibrations is the solar wind.

Absolute sensitivity of the plasma sensors was tested through cross-calibration with the Wind-SWE instrument (Ogilvie et al. 1995). Electron densities measured by THEMIS THC and THD in the solar wind were compared with SWE proton densities, with appropriate corrections for time delays based on the location of the Wind spacecraft. Five intervals during a two month period were compared and a ~ 0.7 correction to the THEMIS densities was required to give good agreement. Figure 15 shows an example of this cross-calibration. The top panels show the THC and THD electron spectrograms with nearly identical solar wind plasma. The black lines indicate spacecraft potential, $e\Phi_{sc}$. The third panel shows the IMF magnitude (Wind-black, THC-red, and THD-green) which assists in the determination of the temporal alignment and the verification of the suitability of the time interval. The bottom panel demonstrates that the Wind-SWE, THC and THD densities have good agreement after the correction factor is applied. Since $e\Phi_{sc}$ was below the lower energy cutoff of the THEMIS electron sensors, this comparison used a density calculation algorithm that extrapolated the distribution function to $e\Phi_{sc}$, assuming a Maxwellian distribution. For the data in Fig. 15, this algorithm introduced a 2% to 9% increase in the calculated the THEMIS electron density relative to a simple algorithm that just used the measured energy range.

The above cross-calibration indicates the THEMIS electron ESA pre-flight geometric factors were underestimated by $\sim 40\% (\sim 1./0.7)$. Recall in Sect. 2.2, the ion sensor energy efficiency was adjusted to account for leakage fields through the exit grid. A similar low-energy efficiency-correction was not performed for electrons since high energy electrons produce secondary electrons at the analyzer exit which can also add to the combined analyzer-detector sensitivity. We assumed the combined effects of the leakage fields were flat in energy and would be determined when the overall geometric factor was calibrated. It now seems likely that the above 40% correction is at least partly due to these leakage fields. Part of the correction may also be due to an underestimate of the MCP detection efficiency (we assumed 70%). For the five intervals tested, the correction factor was relatively constant and showed no systematic change in time. Temporal variations between the measurements indicate that errors in this cross-calibration are at the $\sim 10\%$ level. The 40% correction fac-

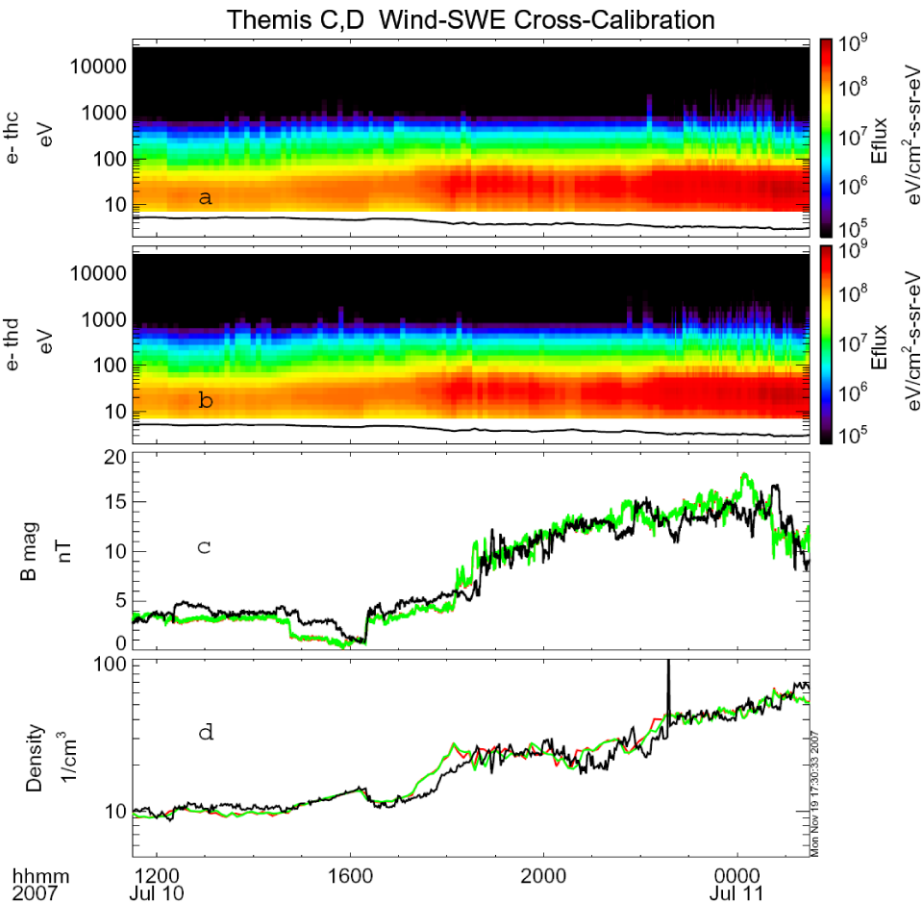

Fig. 15 Plot illustrates the cross calibration between Wind-SWE and THEMIS electron ESAs used to determine absolute sensitivity. The plot shows electron spectrograms from THC (panel **a**) and THD (panel **b**) in the solar wind. Panel **c** shows the IMF magnitude on Wind (*black*), THC (*red*) and THD (*green*). Panel **d** shows the agreement between ion density on Wind (*black*), and electron density on THC (*red*) and THD (*green*) after the cross calibration. Since THC and THD measurements of IMF and density are nearly identical, only the green curve (THD) shows in panels **c** and **d**

tor was combined with the pre-flight sensor geometric factors to obtain the absolute sensor geometric factors.

As a final test of the absolute calibration, magnetopause crossings were evaluated to check for pressure balance. Figure 16 shows an example that contains several magnetopause crossings in addition to flux transfer events. The bottom panel shows the electron (red), ion (green), and magnetic (blue) pressures, in addition to the combined pressure (black). The nearly constant total pressure during these crossings indicates accurate absolute calibrations.

3 Summary

The THEMIS ESA plasma instrument measures the 3-D distribution functions of electrons (up to 30 keV) and ions (up to 25 keV) using a pair of "top hat" electrostatic analyzers. Parti-

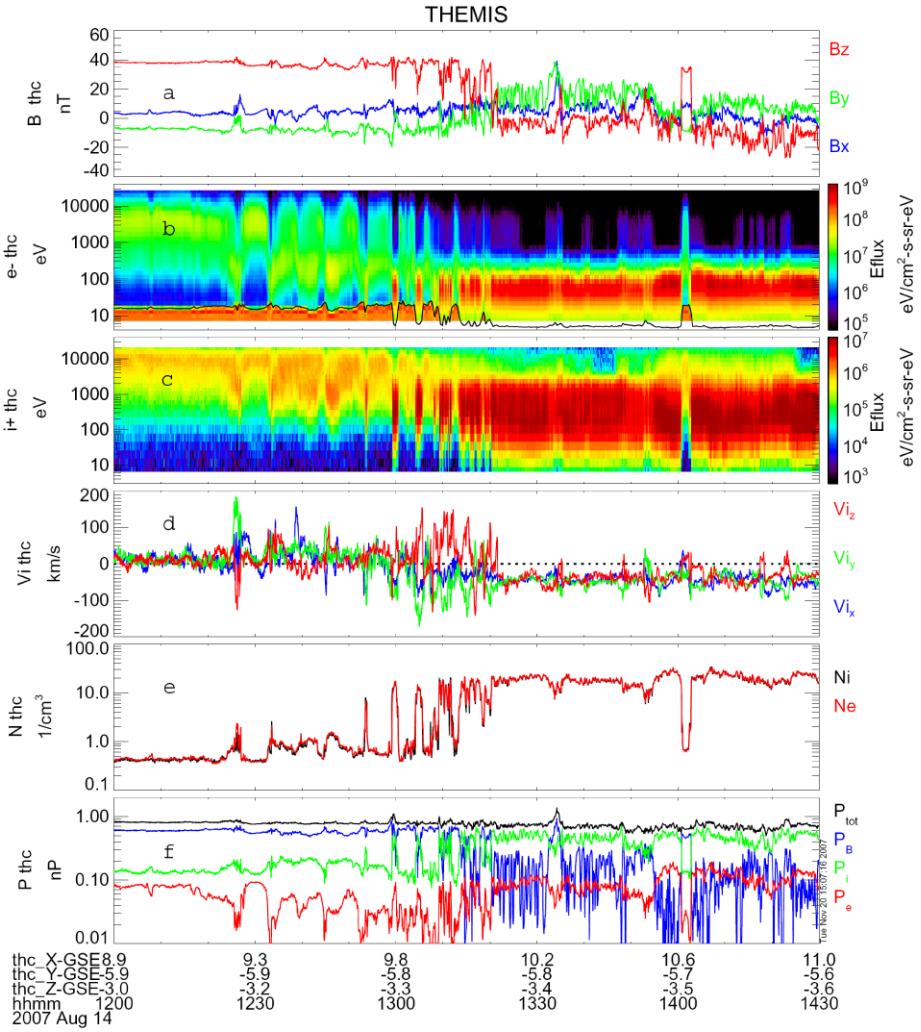

Fig. 16 THEMIS magnetopause crossing used to test calibrations. From top to bottom: magnetic field, electron spectrogram, ion spectrogram, ion velocity, density, and pressure. Good agreement of the electron (*red*) and ion (*black*) densities (panel **e**) indicates good cross-calibration. Nearly uniform pressure (panel **f**) across several magnetopause boundaries, on either side of flux transfer events, and within magnetosheath mirror modes, reveals accurate absolute calibrations

cle events identified by microchannel plate detectors are binned into six types of distributions whose energy, angle, and time resolution depend upon instrument mode. Omni-directional spectra or coarse-angle resolution distributions are continuously available at spin resolution (3 s). Higher energy-angle resolution distributions are available at a lower cadence or at spin resolution during burst data collection. In addition, on-board data processing generates plasma moments at spin resolution that include corrections for spacecraft charging.

The overall design of the THEMIS ESA plasma instrument was directly derived from the FAST Plasma Instrument (Carlson et al. 2001). This modular design simplified assembly and subsystem testing of the 10 flight ESAs. The primary changes from the FAST design

were the development of a resetable closing mechanism that utilizes an SMA actuator to seal the detector from contamination, and the change from gold-black to ebanol-C blacking which reduces scattered sunlight from reaching the detector. Ground calibrations showed the five sensor pairs to be nearly identical in response and all ten sensors continue to perform optimally after 16 months.

The close proximity of the THEMIS satellites during the first 7 months of the mission allowed extremely accurate multi-satellite cross-calibrations of the plasma sensors. These calibrations were facilitated by having all the plasma measurements available with the same resolution and format, along with spacecraft potential and magnetic field measurements in the same data set. The methodology of the in-flight calibration effort has been outlined in this paper, and its precision demonstrated through comparisons with Wind-SWE and total pressure across the magnetopause. However, this calibration effort is not complete. The THEMIS plasma instruments will require monitoring throughout the mission to track and quantify degradation of the MCP detectors and to determine the adjustments to their bias voltages. Future tracking and calibration efforts will utilize the same methods employed above, but will be more difficult due to larger spacecraft separations. It is envisioned that additional cross-calibration efforts will rely on the few month period each summer when multiple satellites encounter the solar wind. Lessons learned from this effort should be useful for future multi-satellite missions.

Acknowledgements The analysis of THEMIS data was supported by NASA NAS5-02099. We thank J. Bonnell and F. Mozer for providing spacecraft potential, and K.-H. Glassmeier for providing magnetic field data. These data assisted the ESA in-flight calibration effort. Financial support for the work of the FGM Lead Investigator Team at the Technical University of Braunschweig by the German Ministerium für Wirtschaft und Technologie and the Deutsches Zentrum für Luft- und Raumfahrt under grant 50QP0402 is acknowledged.

References

V. Angelopoulos, Space Sci. Rev. (2008). doi:10.1007/s11214-008-9336-1

H.U. Auster, K.H. Glassmeier, W. Magnes, O. Aydogar, D. Constantinescu, D. Fischer, K.H. Fornacon, E. Georgescu, P. Harvey, O. Hillenmaier, R. Kroth, M. Ludlam, Y. Narita, K. Okrafka, F. Plaschke, I. Richter, H. Schwarzi, B. Stoll, A. Valavanoglu, M. Wiedemann Space Sci. Rev. (2008). doi:10.1007/s11214-008-9365-9

J.W. Bonnell, F.S. Mozer, G.T. Delory, A.J. Hull, R.E. Ergun, C.M. Cully, V. Angelopoulos, P.R. Harvey, Space Sci. Rev. (2008, this issue)

C.W. Carlson, D.W. Curtis, G. Paschmann, W. Michael, Adv. Space Res. **2**, 67–70 (1983)

C.W. Carlson, J.P. McFadden, P. Turin, D.W. Curtis, A. Magoncelli, Space Sci. Rev. **98**, 33–66 (2001)

R.R. Goruganthu, W.G. Wilson, Rev. Sci. Instrum. **55**(12), 2030 (1984)

R.S. Gao, P.S. Gibner, J.H. Newman, K.A. Smith, R.F. Stebbings, Rev. Sci. Instrum. **55**(11), 1756 (1984)

P.R. Harvey, E. Taylor, R. Sterling, M. Cully, Space Sci. Rev. (2008, this issue)

D. Larson, T. Moreau, R. Lee, R. Canario, R.P. Lin, Space Sci. Rev. (2008, this issue)

J.P. McFadden, C.W. Carlson, D. Larson, J. Bonnell, F. Mozer, V. Angelopolos, K.-H. Glassmeier, U. Auster, Space Sci. Rev. (2008, this issue)

K.W. Ogilvie, D.J. Chorney, R.J. Fitzenreiter, F. Hunsaker, J. Keller, J. Lobell, G. Miller, J.D. Scudder, E.C. Sittler Jr., R.B. Torbert, D. Bodet, G. Needell, A.J. Lazarus, J.T. Steinberg, J.H. Tappan, A. Mavretic, E. Gergin, Space Sci. Rev. **71**, 55–77 (1995)

A. Pederson, F. Mozer, G. Gustafsson, in *Measurement Techniques in Space Plasmas: Fields*. Geophysical Monograph, vol. 103, (1998), p. 1

A. Roux, O. Le Contel, C. Coillot, A. Bouabdellah, B. de la Porte, D. Alison, S. Ruocco, M.C. Vassal, Space Sci. Rev. (2008, this issue)

D.G. Sibeck, V. Angelopoulos, Space Sci. Rev. (2008). doi:10.1007/s11214-008-9393-5

H.C. Straub, M.A. Mangan, B.G. Lindsay, K.A. Smith, R.F. Stebbings, Rev. Sci. Instrum. **70**(11), 4238 (1999)

E. Taylor P. Harvey, M. Ludlam, P. Berg, R. Abiad, D. Gordon, Space Sci. Rev. (2008, this issue)